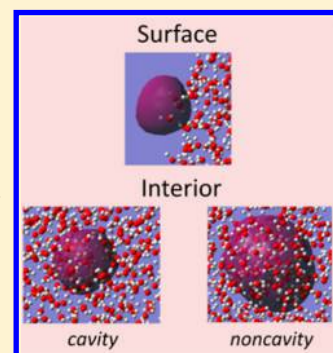


# Hydrated Electrons in Water Clusters: Inside or Outside, Cavity or Noncavity?

László Turi\*

Department of Physical Chemistry, Eötvös Loránd University, P.O. Box 32, Budapest 112, H-1518 Hungary

**ABSTRACT:** In this work, we compare the applicability of three electron–water molecule pseudopotentials in modeling the physical properties of hydrated electrons. Quantum model calculations illustrate that the recently suggested Larsen–Glover–Schwartz (LGS) model and its modified m-LGS version have a too-attractive potential in the vicinity of the oxygen. As a result, LGS models predict a noncavity hydrated electron structure in clusters at room temperature, as seen from mixed one-electron quantum–classical molecular dynamics simulations of water cluster anions, with the electron localizing exclusively in the interior of the clusters. Comparative calculations using the cavity-preferring Turi–Borgis (TB) model predict interior-state and surface-state cluster isomers. The computed associated physical properties are also analyzed and compared to available experimental data. We find that the LGS and m-LGS potentials provide results that appear to be inconsistent with the size dependence of the experimental data. The simulated TB tendencies are qualitatively correct. Furthermore, ab initio calculations on static LGS noncavity structures indicate weak stabilization of the excess electron in regions where the LGS potential preferably and strongly binds the electron. TB calculations give stabilization energies that are in line with the ab initio results. In conclusion, we observe that the cavity-preferring pseudopotential model predicts cluster physical properties in better agreement with experimental data and ab initio calculations than the models predicting noncavity structures for the hydrated electron.



## 1. INTRODUCTION

The physical chemistry community has witnessed a wave of scientific activity in the past few years concerning an interesting, exotic species: the hydrated electron.<sup>1</sup> Although the hydrated electron, an excess electron in a water bath, is a highly reactive species,<sup>2</sup> it is thought to be an important intermediate in various fields.<sup>3</sup> The scientific relevance of the hydrated electron stems not only from its chemical reactivity, but also from its significance as a simple, yet instructive model system. Beyond scientific research, even basic textbooks can benefit from a pictorial representation of the hydrated electron as a truly quantum particle interacting with its solvent environment (see Figure 3 later). The renewed (or more accurately, continuous) research interest in the species is mainly fueled by experiments employing the most sophisticated laser techniques in the femtosecond<sup>4–11</sup> or even attosecond<sup>12</sup> time regimes and by theoretical attempts to provide tools and arguments to interpret the experimental observations.<sup>13–15</sup>

Molecular dynamics (MD) simulations have proved to be very efficient at rationalizing experimental observations and have converged over time to a more or less consistent picture of the hydrated electron, as reviewed recently.<sup>16</sup> Molecular dynamics on hydrated electrons has been predominantly applied in the one-electron approximation, treating the electron quantum mechanically while modeling the solvent environment with classical force fields<sup>17–20</sup> in a mixed quantum–classical MD (QCMD) framework.<sup>21–23</sup> More recently, many electron ab initio molecular dynamics (AIMD) simulations have also been employed to provide a more precise characterization of the system.<sup>13,24–31</sup> After years of effort, it has recently become

possible to characterize the structure<sup>29,30</sup> and reproduce the absorption spectrum<sup>31</sup> of the hydrated electron using AIMD. There have also been promising efforts to simulate the chemical reactivity of the hydrated electron,<sup>13</sup> a domain that is unreachable for one-electron QCMD techniques. Problems with AIMD, however, still persist in terms of the selection of the electronic structure calculation method,<sup>32</sup> the simulated system size, and the sampling efficiency. These limitations of AIMD equally contribute to the fact that QCMD methods are still widely applied.<sup>16</sup> An excellent recent example of an important application of one-electron QCMD methods, that is forbidden for AIMD treatment, involves free energy calculations for the hydrated electron system from MD simulations.<sup>33</sup>

We note here that the classical approximation of the solvent bath represents the main limitation on the applicability of QCMD techniques. Nevertheless, it has been repeatedly pointed out that the most critical ingredient of QCMD methods determining the physical viability of the simulated properties is the one-electron pseudopotential model that describes the interaction between the classical water bath and the quantum mechanical electron. Most of the conceptually challenging problems on the field were recognized within the context of one-electron QCMD simulations and are all closely related to the applied electron–water molecule pseudopotential.

Received: December 19, 2014

One such prominent problem concerns the structure of the hydrated electron. Although there are reasonable models in the literature that differ in the identification of the hydrated species (i.e., an excess electron,<sup>34</sup> a solvent–anion complex,<sup>35</sup> a hydronium cation–hydroxyl anion complex,<sup>36</sup> a hydronium radical<sup>37,38</sup>), the dominantly accepted, more or less consensus model—the cavity model—proposes that a single electron is localized in a spatial void (cavity) in the water bath surrounded by oriented water molecules.<sup>34,39,40</sup> This model was inferred and examined very early<sup>34</sup> and then later supported by one-electron path-integral Monte Carlo,<sup>41</sup> path-integral molecular dynamics,<sup>40,42</sup> and QCMD simulations.<sup>18</sup> Without completeness, we mention that the early pseudopotentials of Schnitker and Rossky,<sup>43</sup> Barnett et al.,<sup>44</sup> and Staib and Borgis,<sup>23</sup> as well as the more recent models of Turi and Borgis<sup>45</sup> and Jacobson and Herbert<sup>46</sup> all lead to cavity structures in QCMD simulations. The recently developed pseudopotential of Larsen, Glover, and Schwartz (LGS) resulted in a completely different type of electron distribution, namely, a noncavity-type structure for the bulk hydrated electron.<sup>47</sup> In the noncavity (“inverse plum pudding”<sup>48</sup>) model, the electron is distributed over several water molecules in a region of enhanced water density. The electron can also localize in cavities, but these voids are short-lived, collapsing and then re-forming very quickly. Inconsistencies in the LGS potential were soon pointed out based on two independent approaches. A quantum mechanical analysis of a simple model and a subsequent quantum simulation showed that the LGS model is too attractive around the oxygen atom, and a simple modification of the potential leads to cavity structures in QCMD simulations.<sup>49</sup> A quantum-chemistry-based analysis pointed out significant deviations between the predictions of the LGS model and the results of *ab initio* benchmark calculations for small static water cluster anions.<sup>50</sup> A comparative study evaluating the applicability of the LGS, Turi–Borgis (TB), and Jacobson–Herbert (JH) models in simulations of the bulk hydrated electron was also published, demonstrating that the basic physical properties associated with the cavity model are in more acceptable agreement with experiments than those computed with the LGS noncavity model.<sup>51</sup> Nevertheless, the application of the LGS model for the calculation of the resonance Raman spectrum of the hydrated electron produced a picture that was consistent with experiment, whereas cavity models seem to fail in this respect.<sup>48</sup>

Another challenging structural issue arises in connection with the presence of interfaces in finite-size hydrated electron systems. It is generally accepted that the experimentally observed distinct patterns of the excess-electron vertical detachment energy (VDE) with cluster size reflect the existence of distinct water cluster anion structural motifs (isomers). However, there is still no consensus on whether the excess electron is localized in the interior or on the surface of the clusters.<sup>10,15,52–59</sup> Clusters with different localization modes (i.e., interior-state clusters vs surface-state clusters) are expected to exhibit different physical properties, as well as different trends of these properties with cluster size. Typical examples are the radius of the excess electron, the optical absorption spectra, and the lifetime of the electronic excited states.<sup>10,15,52,53,57,59</sup> Of the cavity models, the JH and TB models reproduce the experimental VDE tendencies in a semiquantitative manner, but their assignments do not necessarily agree with the tentative experimental assignments.<sup>15,57,59</sup> This unsettled problem provides an ideal testing ground where one can compare and contrast the predictions of

the noncavity LGS model with experiments and with the results of the cavity-preferring potentials. Furthermore, cluster calculations can be related to simulated data on bulk hydrated electrons by extrapolating cluster results to the bulk. This cluster extrapolation approach can be helpful in evaluating and removing artifacts that can be associated with bulk simulations. Potential problems include the application of a finite simulation box with periodic boundary conditions and the neglect or incomplete inclusion of long-range interactions. Such complex comparisons and analyses are the main goals of the present work. Here, we mention that the original LGS pseudopotential was applied to the bulk hydrated electron. However, because the procedure for developing the LGS potential is independent of whether the potential is intended for use in the bulk or in clusters, we propose the extension of the application of the LGS potential to finite-size water cluster anions. The examined cluster sizes include a cluster size ( $n = 1000$ ) that is larger than the system size in the original bulk simulation.<sup>47</sup>

In this work, we evaluate the structural, energetic, and spectroscopic properties of water cluster anions of various sizes computed in QCMD simulations using two pseudopotential models, one predicting a noncavity structure (LGS model) and another with a cavity structure (TB model) in bulk hydrated electrons. The reason for the choice of the latter potential is that both the LGS and TB potentials employ the same nonpolarizable water–water classical potential [simple point charge (SPC) model with flexibility].<sup>60</sup> The differences in the simulated properties of the hydrated electron must be due to the application of different electron–water molecule potentials. An additional motivation for the direct comparison of these two potentials is that both were developed on the same theoretical footing applying one-electron static-exchange (SE) pseudopotential theory. The conclusions of the molecular dynamics simulations are also supported by *ab initio* calculations on structures extracted from the MD runs. To further facilitate the present analysis, we also perform simulations with a slightly modified version of the LGS model (m-LGS) with a polarization parameter that is similar to that in the TB model (see details later). We also note that we recently published a brief comparison of electron hydration dynamics in water clusters using the TB and LGS models.<sup>61</sup> In that study, we found a unique dynamical signature that is associated with the cavity collapse following electron removal from water cluster anions in the TB model (but not in LGS simulations). We suggested that this effect might be experimentally observable.<sup>61</sup>

The aim of the present work is to provide a more general analysis and comparison. In this context, we are aware that pseudopotentials that treat solvent polarization explicitly have been developed and published recently (the JH potential<sup>46</sup> and the self-consistent polarization potential of the Jordan group<sup>62</sup>). Although we acknowledge the merits of these models, for the reasons discussed above, we omit them from the present comparison.

The structure of this article is as follows: In section 2, we briefly compare and analyze the main features of the two pseudopotentials based on a simple quantum mechanical model. Section 3 collects the QCMD simulation results and compares the predictions of the three different electron–water molecule pseudopotential models. Section 4 contains a limited set of illustrative *ab initio* calculations on cluster structures taken from the molecular dynamics trajectories. Section 5 provides a discussion and concludes the article.

## 2. PSEUDOPOTENTIALS

The development of both pseudopotential models was based on the one-electron static-exchange (SE) pseudopotential approximation.<sup>63</sup> In the SE procedure, one solves the Schrödinger equation for an excess electron in the field of the frozen wave function of a single water molecule:<sup>43</sup>

$$H|\Psi\rangle = (T + V_n + V_e + V_x + V_r)|\Psi\rangle \quad (1)$$

where  $T$  is the kinetic energy operator and  $V_n$ ,  $V_e$ , and  $V_x$  are the static nuclear attraction, the static electronic Coulomb repulsion, and the nonlocal exchange, respectively. The repulsion operator ( $V_r$ ) is introduced in eq 1 to account for the orthogonality of the occupied orbitals of the water molecule and the wave function of the excess electron. Following the Phillips–Kleinman (PK) theorem<sup>64</sup> and the work of Cohen and Heine,<sup>65</sup> it is then possible to solve eq 1 and obtain the exact pseudowave function,  $\Psi$ . In practice, this is achieved by the minimization of the kinetic energy of the excess electron with respect to small linear coefficients of the occupied (core) orbitals ( $\varphi_c$ ) that are mixed with the  $\varphi_v$  valence orbital [lowest unoccupied molecular orbital (LUMO)] of the water molecule.<sup>45</sup>

$$|\Psi\rangle = (|\varphi_v\rangle + \sum_c b_c |\varphi_c\rangle) / (1 + \sum_c |b_c|^2) \quad (2)$$

The pseudowave function conserves the eigenvalue and the asymptotic behavior of the exact valence orbital. The pseudopotentials (if exact) should recover this behavior. Both the TB and LGS pseudopotentials used the same procedure above to obtain  $\Psi$ , but the actual developments of the potentials were different. Turi and Borgis introduced a smooth potential that reproduced the asymptotic electron density of the pseudowave function as closely as possible (by minimizing the difference between the exact density and the density predicted by the given potential),<sup>45</sup> whereas Larsen et al. directly constructed the pseudopotential from the pseudowave function and then smoothed and fitted this “exact” potential.<sup>47,66</sup>

The different fitting procedures have important physical consequences. In the TB approach, one can constrain the parameter fitting of the potential to solutions that closely approximate the eigenvalue of the SE Schrödinger equation (eq 1). The direct fitting of the exact potential in the LGS model does not follow this constraint of the PK pseudopotential theory. Thus, although the fitted analytical function in the LGS model is apparently more flexible, containing 16 optimized parameters of 8 Gaussian-type functions, whereas the TB model applies only 4 error functions with 8 parameters, it is the TB model that reproduces the SE eigenvalue of the water molecule + electron model system.

Before the eigenvalues and wave functions of the two pseudopotentials are compared, the quantum mechanical model, namely, a water molecule and an excess electron evaluated within the SE approach, also needs further consideration.<sup>67</sup> Because a single water molecule is not able to bind an excess electron, it is only the finite size of the basis set that keeps the electron in the vicinity of the water molecule in incomplete-basis calculations. The application of large diffuse basis functions (such as those used to generate the pseudowave function in the development of the two pseudopotentials) leads to a delocalized excess electron distribution, mainly outside the water molecule. The excess electron density in the chemically relevant region, in the vicinity of the water molecule, becomes

extremely depleted. This diffuse, small-amplitude electron distribution makes it difficult (and uncertain) to precisely determine the features of the exact underlying potential, as will be seen below. This problem can be diminished through the application of a repulsive confining potential that artificially concentrates the excess electron density in the relevant molecular region, as we proposed some time ago<sup>67</sup>

$$V_{\text{conf}} = \frac{1}{2}k(x^8 + y^8 + z^8) \quad (3)$$

The potential was placed at the center of mass of the water molecule with  $k = 10^{-8}$  au. The steep repulsive walls and the flat central region of the potential ensure that the electron remains localized and that the potential is not altered considerably around the water molecule. The effect of the confining potential on the exact pseudowave function is clearly illustrated in Figures 1 and 2 of ref 67, showing a 2-orders-of-magnitude difference in the confined versus nonconfined densities. Of the two models, the TB potential was developed using a confining potential, whereas the LGS model used a nonconfined potential. For a direct comparison, we performed SE calculations using both pseudopotentials with and without the confining potential with the computational details described in ref 49.

First, we start with the exact solution of the Schrödinger equation. The exact ground-state eigenvalue of an unbound excess electron in the presence of the frozen water molecule wave function is  $1.1973 \times 10^{-3}$  hartree. The energy of the electron, evaluated with the same finite basis set, becomes  $1.3596 \times 10^{-3}$  hartree in the absence of the water molecule. This indicates that, overall, the water molecule slightly attracts the excess electron. The ground-state energy of the exact model using the confining potential around the water molecule changes to  $5.0257 \times 10^{-2}$  hartree.<sup>49</sup> Comparison with the ground-state energy of the free electron in the confining potential ( $4.6585 \times 10^{-2}$  hartree) indicates that the potential in the vicinity of the water molecule is overall repulsive.<sup>49</sup> The net attraction in the nonconfined case is then clearly due to the long-range regions of the exact potential outside the molecular core. Next, we solve the Schrödinger equation for the excess electron in the field of the pseudopotentials with and without the confining potential. This step provides a direct test of the performance of the pseudopotential models. Whereas using the TB potential results in a  $5.0282 \times 10^{-2}$  hartree ground-state energy for the excess electron in the confined case, in excellent agreement with the above exact number, the LGS potential shows a significant deviation with  $4.5725 \times 10^{-2}$  hartree.<sup>49</sup> For the nonconfined problem that tests the asymptotic behavior, one obtains  $1.1829 \times 10^{-3}$  hartree with the TB model and  $1.2298 \times 10^{-3}$  hartree with the LGS potential. The reasonably good agreement of the TB eigenvalue with the exact value for the nonconfined case ( $\sim 1\%$  error) illustrates that the application of the confining potential in the pseudopotential development procedure does not affect the derived pseudopotential considerably. For the LGS method, the confined eigenvalue is  $\sim 9\%$  too low (attractive), and the nonconfined eigenvalue is  $\sim 3\%$  high. Because the electron is expected to localize near the water molecules in condensed-phase simulations, the result for the confined case is disturbing. Here, we reiterate that the LGS model replaces the originally overall repulsive exact potential with a (slightly) attractive interaction (relative to the free electron model in the confining potential).<sup>49</sup>



The excess electron density around the water molecule reflects the properties of the underlying pseudopotentials. Here, we show projections of the electron density of the exact pseudowave function and the densities computed with the TB and LGS models in the molecular plane along the dipole and OH bond directions (Figure 1). At the outset, it can be seen

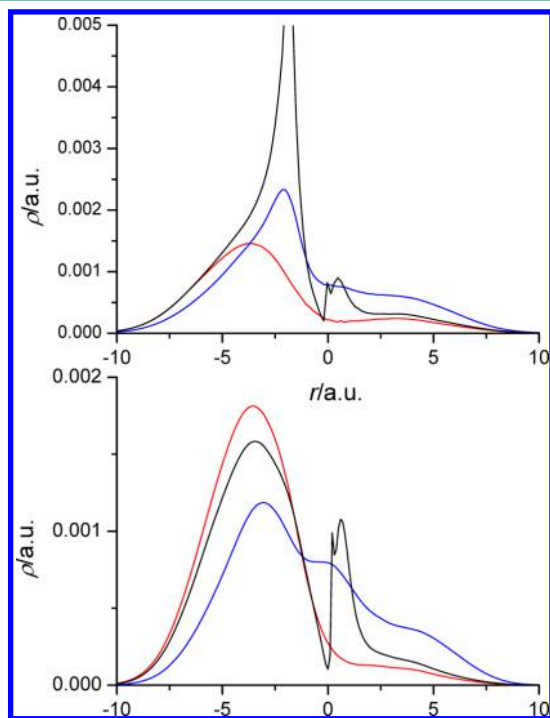


**Figure 1.** Electron density of the exact pseudowave function (black), the LGS electron density (blue), and the TB electron density (red) along the dipole direction in the molecular plane through the oxygen atom (top) and along the OH bond (bottom). The center of mass of the water molecule is at the origin; the hydrogen atoms are at negative coordinates.

that both potentials represent approximations to the exact pseudodensity. Whereas the TB model does a fairly good job at reproducing the asymptotic decay of the exact solution, the deviation of the LGS model is clearly observable. Considering the core behavior, the LGS model does a better job in the vicinity of the hydrogen atoms, whereas the TB model is more reasonable in the dipole direction. We also note that, in both density projections, the LGS model predicts a significant density increase on the oxygen side of the molecule. This feature is due to the fact that an attractive potential region appears behind the oxygen atom that we find to be unusual and hard to reconcile with basic chemical concepts.<sup>49</sup> The artificial increase in LGS density on the oxygen side is associated with a depletion of the density on the hydrogen side of the molecule, as clearly seen in Figure 1. Here, one must also make an additional point regarding the relation of the exact pseudowave function and the LGS potential development procedure. Larsen et al. claimed to generate the exact potential and fit this potential with a suitable set of functions,<sup>47,66</sup> but at the end, there seems to be a deviation between the asymptotic exact density and the LGS density.

Both the LGS and TB models apply a polarization potential that is added to the SE potential a posteriori, in an ad hoc manner.<sup>45,47</sup> Whereas the LGS model uses<sup>47</sup> the polarization potential of Schnitker and Rossky<sup>43</sup>

$$V_{\text{pol}} = -\frac{\alpha}{2r^4} \{1 - \exp[-(r/r_c)^6]\} \quad (4)$$

the TB model applies<sup>45</sup> the polarization of Barnett et al.<sup>44</sup>

$$V_{\text{pol}} = -\frac{\alpha}{2(r^2 + C^2)^2} \quad (5)$$

In eqs 4 and 5,  $\alpha$  is the spherical polarizability of the water molecule (9.7446 au),  $r$  is the electron–oxygen site distance, and  $r_c = 1.53$  Å and  $C = 4.4$  au are cutoff distances.<sup>43,45,47</sup>

Because the LGS potential predicts a too-deep ground-state energy for the hydrated electron in the bulk,<sup>47,49</sup> in the present work, we attempt to weaken the polarization potential, similarly to that used in the TB potential

$$V_{\text{pol}} = -\frac{\alpha}{2(r^2 + C^2)^2} \{1 - \exp[-(r/r_c)^6]\} \quad (6)$$

The modified LGS potential with the polarization of eq 6 is denoted as m-LGS in the remaining of the article. The static-exchange parts of the LGS and TB potentials are shown in the dipole direction and along the OH bond in Figure 2. Figure 2 also contains the polarization potentials for the three investigated models.

### 3. SIMULATION DETAILS AND RESULTS

The simulations were performed using a mixed quantum–classical molecular dynamics method (QCMD)<sup>22</sup> that was developed and successfully employed in the Rossky group (see references in ref 16). Because this technique was also used by us previously in a series of studies,<sup>15,45,49,57,58</sup> we focus only on its main features here. In the present QCMD framework, the interaction between the classical water molecules is given by a flexible three-site potential (SPC + flex),<sup>60</sup> whereas the excess electron is described by its wave function. The wave function is represented on a finite grid, evenly distributed in a cubic box. For the TB potential, we use a cubic grid with a box side of 18.17 Å with  $16 \times 16 \times 16$  equidistant grid points. Because of the more rugged features of the potential surface, the evaluation of the LGS potential requires a denser spatial grid. For this purpose, a grid box of 18.17 Å length with  $32 \times 32 \times 32$  grid points proved to be sufficient. The electron–water molecule interaction is modeled by a pseudopotential, either the TB potential<sup>45</sup> or the LGS potential.<sup>47</sup> The time-independent Schrödinger equation for the excess electron is solved in the potential field of the classical water molecules using an iterative and block Lanczos procedure.<sup>22</sup> The time evolution of the classical subsystem is dictated by the sum of a quantum force (from the electron) and a classical force (from the other molecules). The quantum force is evaluated by applying the Hellman–Feynman theorem. The dynamics is adiabatic. We used the Verlet algorithm to integrate the equations of motion with a time step of 1 fs.<sup>68</sup> The simulated water clusters contained  $n = 45, 66, 104, 200, 500$ , and 1000 water molecules. The simulations were carried out in the microcanonical ensemble. The trajectories were equilibrated at two different effective temperatures: 200 and 298 K. The former was used to compare the simulation results to low-temperature cluster measurements, whereas the 298 K data were used for the extrapolation to bulk hydrated electron properties at ambient conditions. The analysis of the results is based on 50-ps-long equilibrium trajectories for all cluster sizes, pseudopotentials, and temperatures.

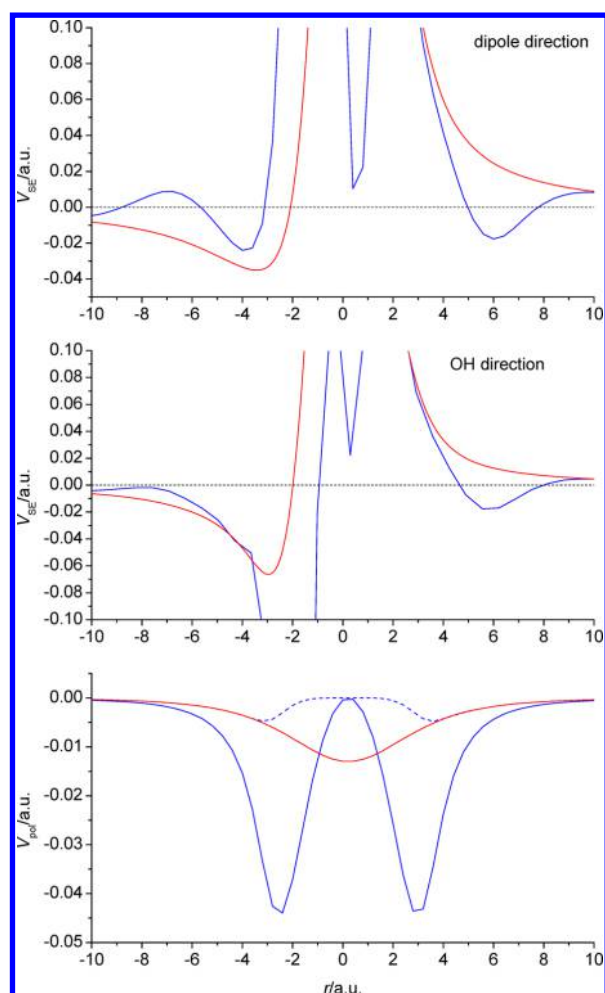


**Figure 2.** Static-exchange potential of the LGS potential (blue) and TB potential (red) along the dipole direction in the molecular plane through the oxygen atom (top) and along the OH bond (middle). The bottom panel shows the polarization contributions to the full potential for the LGS (blue), TB (red) and m-LGS (blue dashed) models. The origin for the dipole direction is the center of mass of the water molecule (top), the oxygen atom for the OH direction (middle), and the polarization potential (bottom). The hydrogen atoms are at negative coordinates.

First, we examine the structural properties of the hydrated electron clusters. The first observation concerns the position of the equilibrated electron relative to the molecular framework of the cluster (Figure 3). According to our previous simple criterion, an electron is localized in the interior of the cluster if  $R + r_e < r_c$ , where  $r_e$  is the radius of gyration of the excess electron ( $r_e = \langle r^2 \rangle^{1/2}$ ),  $r_c$  is the radius of the cluster, and  $R$  is the distance between the centers (centers of mass) of the two distributions.<sup>15,57</sup> For surface-bound states, one has  $R \approx r_c$ . For the TB model, we find two main cluster types (Figure 3). Initial electron attachment to equilibrated neutral clusters and the following relaxation always result in surface-state excess electron distributions at 200 K.<sup>57,58</sup> Trajectories at 200 K launched from neutral clusters with preformed cavities persist in interior-state structures for cluster sizes of roughly  $n \geq 200$  for the typical length of such trajectories, several hundred picoseconds. At higher temperature, 298 K, whereas cluster anions relax into a surface state after electron attachment for  $n = 45$ –200, larger clusters ( $n = 500, 1000$ ) show an increased tendency for the electron to diffuse spontaneously into the

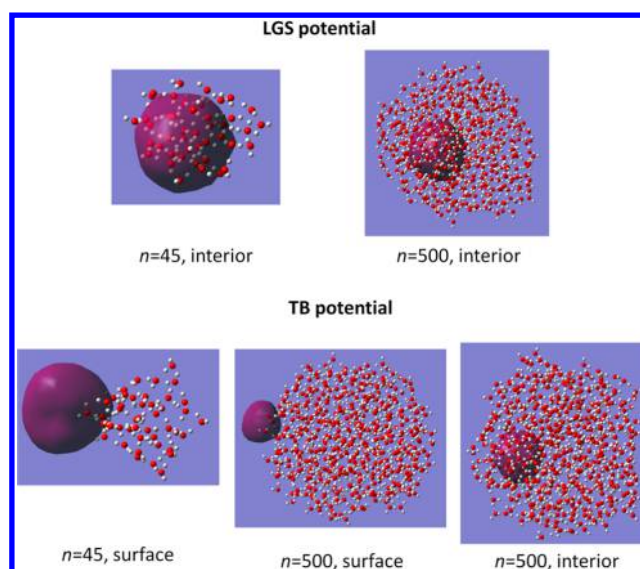


**Figure 3.** Electron density isosurfaces of the excess electron in water cluster anions as calculated with the LGS (top) and TB (bottom) models at 200 K. The isosurfaces show 80% probability of finding the excess electron.

interior of the cluster.<sup>57</sup> The results are more monotonic for the LGS and m-LGS models. For all cases, regardless of the size or the temperature of the clusters, excess electron initial localization and relaxation take place in the interior of the neutral cluster (Figure 3). In addition to the scenario of electron attachment to neutral clusters, we also tested electron localization with the LGS potential starting from configurations that supported surface states in the TB model (preformed TB surface-state clusters). We found that all of these clusters also collapse to interior-state structures within less than  $\sim 1$  ps using both the LGS and m-LGS models. The contrast of the TB and LGS models is also illustrated by the geometrical parameters, as seen in Figure 4 for a relatively small cluster size,  $n = 104$ , at  $T = 200$  K. At this size, the TB model predicts a surface-state isomer, whereas both LGS models prefer an interior state, as

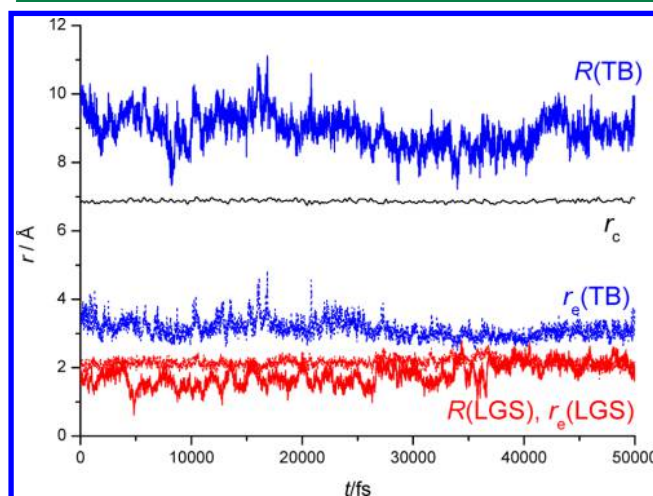


**Figure 4.** Equilibrium time evolution of the radius of the electron ( $r_e$ ), the radius of the cluster ( $r_c$ ), and the distance between the center of mass of the water cluster and the center of mass of the excess electron ( $R$ ) at  $T = 200$  K in  $n = 104$  water cluster anions. Red shows the results using the LGS model; blue indicates TB simulations.

demonstrated by the evolution of the  $R$  parameter. As expected, the surface-state electron (TB) is more diffuse than the interior-state electron in LGS simulations (see parameter  $r_e$ , the radius of the excess electron, in Figure 4). At larger cluster sizes, whereas interior-state isomers can also appear using the TB model, the LGS models still predict interior-state electron distribution. We analyze the cluster size dependence of the size of the excess electron later. Here, we note that the relative position of the excess electron with respect to the cluster can also depend on the cluster preparation method, as was illustrated by one-electron pseudopotential (TB)<sup>69</sup> and AIMD simulations.<sup>70</sup> As an additional comparison, another one-electron pseudopotential (JH) that simulates cavity structure for the bulk hydrated electron predicts four types of cluster anion isomers depending on cluster size, temperature, and cluster preparation using different geometric criteria.<sup>59,71</sup>

Next, we characterize the local water structure surrounding the electron. The solvent structure (around the solute) and the solute structure (the excess electron distribution in the water bath) are mutually determined by the electron–water molecule interaction. The LGS and TB models predict conceptually different excess electron states in the bulk and different solvent structure in the vicinity of the electron. Whereas the TB model results in a cavity-type structure,<sup>45</sup> the LGS model simulates a noncavity electron distribution.<sup>47</sup> The relative position of the electron distribution with respect to the cluster interfaces can further complicate the structural details of water cluster anions.

The TB model does indeed fall into this category, with at least two isomeric water cluster anion groups. Figure 5 shows the electron center-of-mass–oxygen site and the electron center-of-mass–hydrogen site radial distribution functions (RDFs) for clusters of selected sizes computed with the TB model at 200 K. At this temperature, both interior and surface excess electron states can be realized depending on the cluster size. For both types of isomers, one can observe an excluded volume around the electron in the distribution functions. The position of the first maximum appears rather uniformly at  $\sim 2$  Å for the hydrogen RDF and  $\sim 3$  Å for the oxygen RDF, consistent with bond-directed water orientation toward the electron, similar to that found in bulk.<sup>45</sup> The similar positions of the maxima and the relative intensity of the RDFs for the interior-state clusters relative to those for surface-state clusters of the same size ( $\sim 1.5$ – $1.8$  for the  $n = 500$  and  $1000$  cases) suggest that surface-state excess electrons localize in dents on the surface, nearly in a half-cavity. As the clusters grow, the dent gradually forms and becomes deeper, indicated by the increasing intensity of the first maximum of surface-state clusters with size. We also find that smaller clusters have more diffuse radial distribution functions, consistent with weaker electron–cluster interactions. This leads to a more diffuse electron distribution and, at the same time, easier penetration of the OH group into the electron cloud. This effect is most prominent at the smallest cluster sizes ( $n < 66$ ), where one observes shrinking excluded volumes and shifting maxima of the RDFs toward the center of the electron.<sup>72</sup> Increasing the temperature (to  $T = 298$  K) does not alter the major tendencies, except in two respects. The RDF functions (not shown) become somewhat less structured at higher temperature, and the size of the excluded volume, although its presence is apparent, shrinks. We also note that, because surface-state electrons diffuse to the interior of the cluster for  $n = 500$  and  $1000$  clusters, direct comparison of interior-state

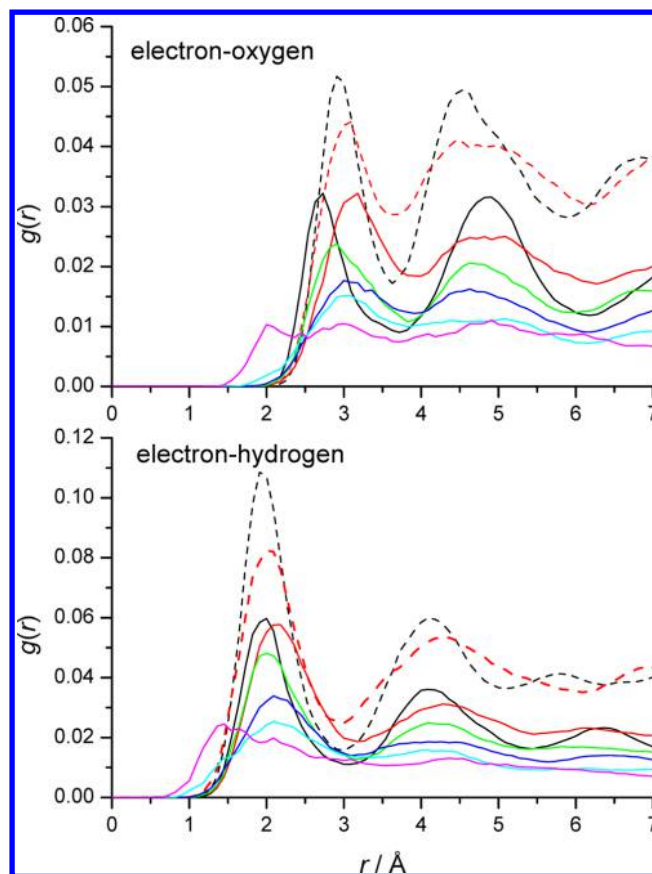


**Figure 5.** Electron center-of-mass–oxygen and electron center-of-mass–hydrogen radial distribution functions simulated with the TB model at 200 K in water cluster anions. The cluster sizes are  $n = 45$  (magenta), 66 (cyan), 104 (blue), 200 (green), 500 (red), and 1000 (black). Surface-state clusters are indicated by solid lines, interior-state clusters by dashed lines.

clusters with surface-state clusters of the same size is not possible at 298 K.

The structural predictions of the LGS model at 298 K for clusters strongly parallel the results found for the ambient bulk hydrated electron with the same model.<sup>47</sup> No cavity is formed for the interior stabilized excess electron, as indicated by the apparent lack of the excluded volume in the pair correlation functions of the clusters (Figure 6). The maxima (approximately identical to the bulk 298 K data) appear at  $\sim 1$  Å for the hydrogen RDF and  $\sim 2$  Å for the oxygen RDF (not shown), irrespective of the cluster size. For the 200 K LGS cluster anions, the sign of tiny cavities (with small excluded radius,  $\sim 0.5$  Å) becomes visible (Figure 6). This suggests that the water kinetic energy is not sufficient to collapse the cavity below ambient temperatures in the LGS model. The m-LGS model predicts a significantly weaker interaction of the electron with the water molecules because of its scaled-down polarization part (eq 6). Still, the m-LGS radial distribution functions are not very different from those computed with the LGS model. Interestingly, although the hydrogen radial distribution functions in the m-LGS simulations indicate a noncavity structure, the directional preference of the OH bonds toward the electron essentially disappears at 298 K. At lower temperatures ( $T = 200$  K), both the hint of the cavity character and the OH directionality reappear in m-LGS simulations (Figure 6).



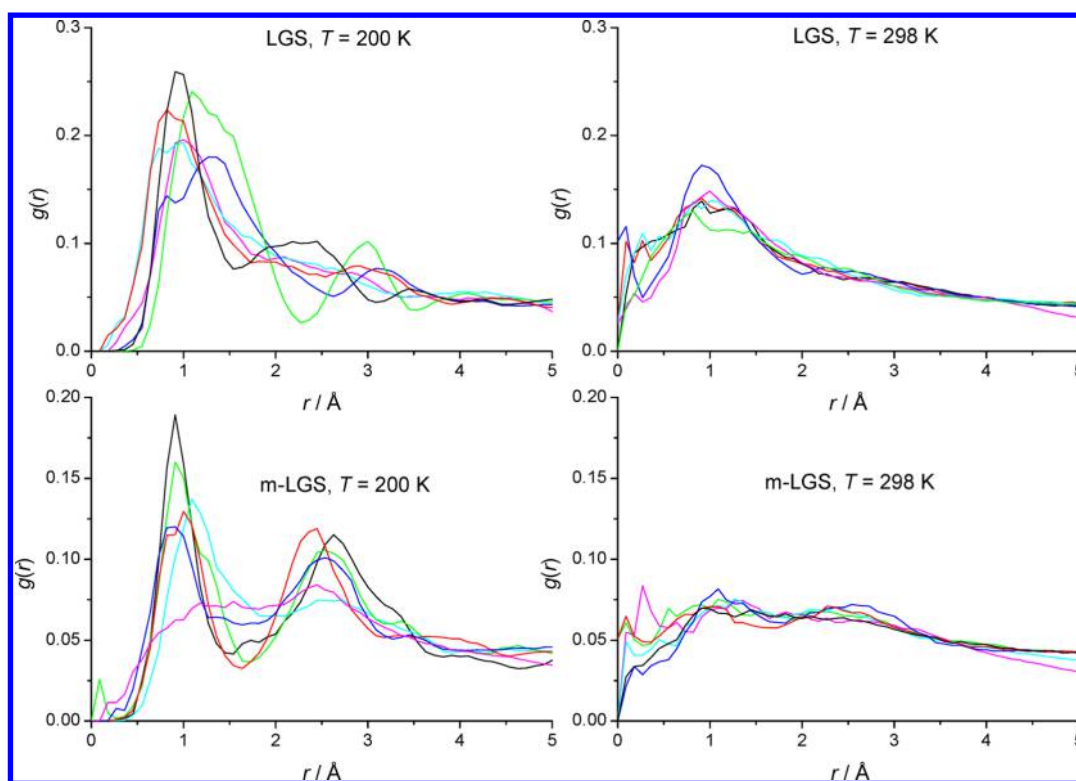


**Figure 6.** Electron center-of-mass–hydrogen radial distribution functions simulated with the LGS and m-LGS models at 200 and 298 K in water cluster anions. The cluster sizes are  $n = 45$  (magenta), 66 (cyan), 104 (blue), 200 (green), 500 (red), and 1000 (black). All clusters are interior-state clusters.

The next analyzed characteristic structural property is the radius of the electron. Using spectral moment analysis of absorption spectra, Bartels derived experimental excess electron radius data for size-selected water cluster anions.<sup>52</sup> The data evaluation of Bartels suggests that, as the cluster size grows, the size of the electron distribution shrinks, approaching an asymptotic limit from above. We note that, although the experimentally examined clusters were smaller in size than the present simulated ones, one can expect that the observed trend continues for larger clusters, as well. It was shown previously that the experimental tendency is followed qualitatively by cold (200 K) surface-state isomers in simulations using the TB model.<sup>15,57</sup> Here, we also point out that the size of surface-state electrons appears to be somewhat overestimated in the TB model. Interior-state excess electrons of the TB model have an essentially constant radius (2.36 Å for  $n = 500$  and 1000 interior-state clusters at 298 K), in good agreement with the simulated radius of the ambient bulk hydrated electron (2.42 Å).<sup>15,57</sup> Similar overall tendencies are seen with another recent cavity-predicting pseudopotential, the JH model, that was not examined here.<sup>46,59</sup> Figure 7 collects the simulated radius data at 200 K. The LGS model predicts only interior-state clusters in the examined size range. At 200 K, the radius shows essentially no size dependence, ranging between 2.0 and 2.2 Å. At 298 K, one can observe a moderately increasing tendency from 2.42 Å ( $n = 45$ ) to 2.64 Å ( $n = 1000$ ). Although this latter value is consistent with the simulated radius of the LGS bulk hydrated electron,<sup>47</sup> it slightly exceeds the experimentally inferred radius (2.45 Å at ambient conditions).<sup>53</sup> In addition, the LGS tendencies are at odds with the trend found experimentally for the size dependence of the radius.<sup>52</sup> Test simulations performed below the examined size range ( $n = 20$  and 30

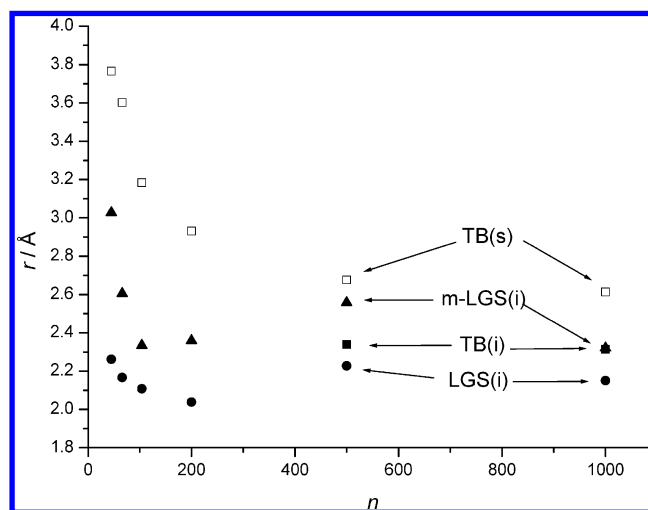


**Figure 7.** Radius of gyration of the excess electron in water cluster anions of various sizes computed at 200 K using the TB model (■), the LGS model (●), and the modified m-LGS model (▲). Open squares show surface-state cluster anions, realized only in the TB model (□).

clusters) also indicate that the above tendencies definitely continue to smaller cluster sizes, as well. We also point out here that the LGS excess electron distributions are comparable in size to those for interior states in TB simulations. This fact shows that both potentials predict localized excess charge distribution, but on different parts of the potential energy surface. Using a weaker polarization interaction in the m-LGS potential results in a radius pattern with size that resembles the experimental tendency. The radii of cold clusters decrease with

cluster size and reach a value (2.32 Å) in the  $n = 1000$  cluster that compares favorably with the ambient bulk radius (Figure 7). At ambient conditions, the clearly decreasing 200 K tendency disappears, and one observes a delocalized excess electron structure with a radius of  $\sim 4$  Å in the largest examined clusters.

Now, we turn our attention to the energetic and steady-state spectroscopic data of water cluster anions. The experimental vertical detachment energy (VDE) data for water cluster anions reflect characteristic trends with size,<sup>10,54</sup> and reasonable models are expected to capture these qualitative features. Figure 8 contains the computed VDE data as a function of

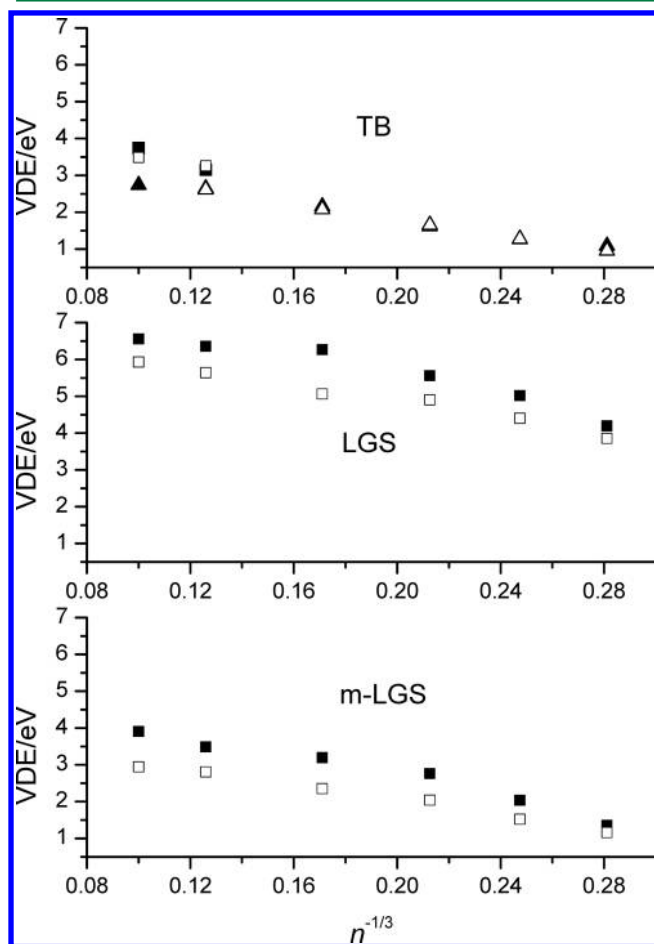


**Figure 8.** Vertical detachment energy of the excess electron in water cluster anions of various sizes computed using the TB model, the LGS model, and m-LGS model at 200 K (solid symbols) and 298 K (open symbols). Squares show interior-state cluster anions; triangles indicate surface-state anions.

cluster size. Here, we use the usual  $n^{-1/3}$  representation of the data that is used in dielectric continuum models and leads to an apparent linear behavior.<sup>73</sup> The TB model was previously shown to predict at least two different linear patterns.<sup>15,57</sup> At 200 K, all examined clusters were found to stabilize surface-state excess electron distribution, but interior states were also simulated for clusters with  $n \geq 500$ . Both patterns were also located at a higher temperature (298 K), with surface states persisting up to  $n \approx 500$  and larger clusters stabilizing only in interior states. Interestingly, the TB-computed VDE values did not show a significant temperature dependence in this temperature range.<sup>15,57</sup> Linear extrapolation to  $n^{-1/3} = 0$

provides the simulated bulk limit for the VDE of the hydrated electron. Simulations for interior-state excess electrons gave 4.4 eV, whereas surface-state data extrapolated to 3.9 eV. Both values indicate stronger interactions than the 3.3 eV value extrapolated from cluster measurements<sup>53</sup> and data from direct bulk VDE measurements (3.3,<sup>7</sup> 3.3,<sup>74</sup> and 3.6<sup>75</sup> eV). Furthermore, very low-temperature simulations suggest the possible formation of metastable cluster anions that could appear as another distinct group in the VDE–size diagram.<sup>69,70</sup>

LGS simulations show no sign of the existence of distinct cluster anion isomers for  $n \geq 45$  at the examined 200 and 298 K temperatures.<sup>72</sup> In addition, for the only localized isomer type, the interior-state isomer, the LGS model predicts a significantly stronger binding energy than the experimental VDE range and the TB potential. For example, the VDE of the  $n = 1000$  cluster anion with an interior excess electron is  $\sim 3.5$  eV in TB calculations, whereas it is  $\sim 6.5$  and  $\sim 6$  eV with the LGS model at 200 and 298 K, respectively (Figure 8). Clearly, temperature appears to be an important factor, the 200 K VDE data being significantly greater (by  $\sim 0.6$  eV for the largest clusters) than the 298 K VDE. Thus, although only a single structural isomer type appears in LGS simulations, two patterns of VDE are observable with size, because of a temperature effect. It is also notable that the  $n^{-1/3}$  representation of the data approximately follows linearity. Linear extrapolation to the infinite-size asymptotic limit shows unrealistically high  $\sim 8$  and  $\sim 7$  eV bulk VDE values at 200 and 298 K, respectively. Weakening the polarization part of the LGS potential to be similar to that of the TB potential scales down the VDE values by a factor of  $\sim 2$ , placing them closer to, but not quite within, the experimental data range. The linear character of the VDE– $n^{-1/3}$  function is again approximately correct, with the estimated asymptotic values of  $\sim 5.5$  and  $\sim 4$  eV at 200 and 298 K, respectively.

Finally, we also calculated the optical absorption spectra for the simulated cluster anions. Experimentally, the spectra shift to higher energies with increasing cluster size, apparently extrapolating to a bulk limit.<sup>76</sup> This tendency was illustrated to appear in the surface-state isomers using the TB model, whereas for interior-state clusters, the same model predicts an essentially size-independent position of the spectra.<sup>15,57</sup> With the LGS model at 298 K, smaller clusters have a spectral maximum at  $\sim 1.8$  eV ( $n = 45, 66$ ), whereas larger clusters ( $n = 500, 1000$ ) appear to be slightly red-shifted to  $\sim 1.5$  eV. This latter estimate is consistent with LGS bulk simulation results<sup>47</sup> and thus underestimates the experimental position by  $\sim 0.2$  eV.<sup>77</sup> Similar simulations at 200 K shift the spectra significantly to higher energies, between  $\sim 1.9$  and  $\sim 2.3$  eV. Apparently, no clear size-dependent trend is seen in the evolution of the spectra at either temperature with the LGS potential. The m-LGS model at 200 K gives a tendency that is very similar to the surface-state TB results and experiment, with a clear shift of the position of the spectral maximum from 0.9 eV ( $n = 45$ ) to 1.7 eV ( $n = 1000$ ). The m-LGS 298 K simulations, however, appear to take an opposite trend, progressing from 0.8 eV ( $n = 45$ ) to 0.5 eV ( $n = 1000$ ). The 298 K m-LGS tendency seems to approach an unrealistic large-size limit, and this discredits the otherwise promising tendency at 200 K.

#### 4. AB INITIO CALCULATIONS

To provide a final aspect of the comparison, we performed ab initio calculations on selected water cluster anions that were taken from the QCMD trajectories. We considered two trajectories for the largest cluster size ( $n = 1000$ ) at  $T = 200$



K generated with the LGS and TB potentials, with interior-state excess electron distributions in both cases. From the examined 100-ps-long equilibrium trajectories, we selected 100–100 configurations, separated by 1 ps. From each of the selected configurations, we picked the 12 and 24 water molecules nearest to the center of mass of the excess electron. The 24-molecule model roughly represents the first two solvation shells around the electron. We performed reasonable-quality single-point ab initio calculations on these fixed configurations with and without the excess electron bound to these structures and computed the VDE for each configuration.<sup>78</sup> The calculations were performed using the MP2/6-31(1+3+) $G^*$  level of theory.<sup>79</sup> This method and basis set were tested by Herbert and Head-Gordon<sup>32</sup> and found to be reliable for VDE calculations in the hydrated electron system. We also performed the calculations on the same selected configurations using the LGS and TB potentials.

The cavity structures extracted from TB simulations were observed to be strongly binding by all three methods. MP2 binds the electron by 980 meV, whereas LGS computes 1200 meV, and TB predicts a 630 meV average VDE for the  $n = 12$  configurations. The tendencies are similar for the  $n = 24$  configurations, at 1450 meV (MP2), 2030 meV (LGS), and 1050 meV (TB). For these configuration, LGS overestimates the MP2 value by 0.2–0.6 eV, whereas TB underestimates it by 0.4 eV. We also observe that the LGS binding energy becomes 5.0 eV in the TB cavity structures in the full-cluster ( $n = 1000$ ) limit, whereas TB predicts a value of 3.7 eV.

The noncavity structures generated by the LGS method prove to be very weakly binding using MP2. For the  $n = 12$  configurations, MP2 calculations predict a VDE of only 56 meV. The TB potential predicts a similar VDE, 38 meV. The average LGS stabilization in these structures is unlikely high, 2500 meV. The extent of the deviation is similar for LGS in the  $n = 24$  configurations, with VDEs of 100 meV by MP2, 72 meV by TB, and 3740 meV by LGS. For the  $n = 1000$  limiting case, the LGS value becomes 6.6 eV, whereas the TB calculation predicts 0.87 eV. These findings imply that the LGS model supports such regions of the potential energy surface that are, in fact, not favored in all-electron calculations. This finding appears to be consistent with the observation of quantum model calculations of section 2, where it was concluded that the LGS potential introduces an artificial attraction around the oxygen atom.

We note here that the above computations constitute part of a more general benchmarking study that will be published elsewhere.

## 5. DISCUSSION AND CONCLUSIONS

We examined and compared three electron–water molecule pseudopotential models. The TB and LGS potentials were both developed using the static-exchange theorem with the polarization part added a posteriori. Despite the similar potential development procedures, the two potentials lead to dramatically different structural properties of the hydrated electron. Most notably, whereas the TB model supports the traditional cavity picture of the hydrated electron, the LGS model predicts a noncavity structure with an increased local water density in the vicinity of the excess electron. To separate the effects of the different polarization contributions in the two models, we also examined the LGS potential with a modified polarization (m-LGS potential) that is weakened similar to that used in the TB model. The present analysis focused on three main aspects: (a)

quantum calculations on a model system consisting of one water molecule and an excess electron, (b) adiabatic mixed quantum–classical molecular dynamics simulations on water cluster anions of various sizes using the different pseudopotential models, and (c) illustrative ab initio VDE calculations on structures that were generated in the QCMD trajectories.

Exact quantum model calculations demonstrate that, although the development of the LGS potential was based on the construction of an exact pseudowave function with an exact ground-state eigenvalue and asymptotic behavior, the LGS potential does not conserve these features. In particular, we observed that the LGS potential is overall too attractive, particularly around the oxygen core with the appearance of an attractive region on the oxygen side of the molecule. The TB potential has been shown to predict more consistent agreement with model calculations.<sup>15,57</sup>

Mixed quantum–classical molecular dynamics simulations of water cluster anions using different pseudopotential models were also carried out for further testing purposes. Because direct experimental data exist for bulk hydrated electrons and hydrated electron clusters, comparisons with experiments were used to assess the viability of the potentials. The TB model performs in a semiquantitative manner with respect to experimental cluster geometric, energetic, and spectroscopic data. The potential predicts at least two structural isomers for water cluster anions, namely, interior-state and surface-state clusters. The trends of the radius of gyration, the vertical detachment energies, and the absorption spectra with size reproduce the experimentally observed tendencies. This set of findings has served as a basis for the assignment of the experimental type I clusters as surface-state clusters.<sup>15,57</sup>

The LGS potential predicts the presence of only one isomer type, interior-state clusters. The radius of gyration of the interior-state clusters is similar to that found for the interior-state clusters simulated with the TB model at 200 K. In addition, the radius of the interior excess electron is basically independent of the cluster size in cold clusters. At ambient temperature, the size dependence of the excess electron in LGS clusters is opposite the observed low-temperature experimental tendency, and the electron becomes more diffuse with increasing cluster size. The different tendencies at different temperatures reflect the structural changes in the solvent in the vicinity of the electron. At low temperatures, one observes the formation of a cavity-type solvation structure, whereas at higher temperatures, the structure collapses into the noncavity-type arrangement. LGS simulations also predict a significant overbinding of the excess electron, with VDE values a factor of  $\sim 2$  larger than the experimental data. The VDE does depend on the temperature, as the low-temperature cavity-forming clusters bind the electron  $\sim 1$  eV stronger than the ambient noncavity clusters. The position of the maximum of the absorption spectrum with size also appears to be in disagreement with experiment. Whereas small-cluster experimental spectra show up in the low-energy part of the spectrum ( $\sim 1$  eV), all LGS cluster absorption spectra appear slightly below or beyond the experimental 1.72 eV bulk spectrum at both examined temperatures.

Weakening the polarization part of the m-LGS potential illustrates that most of the unexpected properties of the LGS model originate from the static-exchange part of the potential. Most importantly, the noncavity structure persists in the m-LGS simulations at 298 K, and a decrease in temperature again leads to the reappearance of a tiny cavity. The overbinding

decreases with the scaled-down polarization part, but one still observes a single interior-state isomer of the cluster anions. Simulation results suggest that modification of the polarization part of the LGS potential is not likely to improve the LGS results.

Nevertheless, one cannot leave the topic without discussing the resonance Raman spectrum of the hydrated electron. Figure 4 of ref 48 shows that the spectrum is significantly better reproduced using the noncavity LGS model than the TB model, which predicts neither the shift nor the broadening of the spectrum. This phenomenon clearly points to the limitations of the one-electron approach and the effect of overlap between water occupied orbitals (core orbitals) and the excess electron.<sup>48</sup> Unfortunately, the LGS attempt to remedy this problem leads to the above analyzed inconsistencies in other physical properties. Because both of the examined potentials neglect polarization effects, it would also be desirable to perform the Raman spectrum calculations with the polarizable Jacobson–Herbert model.<sup>46</sup> In addition, to illustrate the complexity of the issue, we also note here that, although this phenomenon clearly calls for AIMD treatment, recent many-electron simulations did not result in a significantly improved spectral shape relative to the LGS model.<sup>29,48</sup>

Ab initio calculations provide a further demonstration of the unusual properties of the LGS potential. Configurations that strongly bind the electron in a noncavity-type arrangement in LGS-generated trajectories are predicted to be only weakly binding using MP2-level ab initio calculations. The ab initio excess electronic densities become very diffuse in these configurations. At the same time, LGS qualitatively predicts the VDEs of cavity-type structures generated by the TB potential. These tendencies are consistent with the observation of our quantum model calculations, namely, that the LGS potential predicts an artificially strong attraction near the oxygen site. Calculations using the TB potential on the same structures reproduce the MP2 trends.

All in all, our analysis suggests that the pseudopotential model of Larsen et al.<sup>47</sup> that results in noncavity structures in bulk hydrated electron simulations predicts cluster anion properties that are, in most of the analyzed cases, not in line with experimental observations and ab initio calculations. The cavity-type TB model that was used for comparison provides a more consistent picture. This is not to say that the analysis proves anything about the structure of the hydrated electron. We simply state that, within the limitations of the models, the cavity-preferring model gives significantly better agreement with cluster experiments than the examined noncavity-predicting LGS model. In terms of the cavity versus noncavity debate, it might be of interest to reiterate here the recent AIMD simulation work of Jungwirth et al.,<sup>29</sup> who found clear signature of the cavity structure in their extended bulk simulations. Although their predicted excluded volume is somewhat smaller than that in the TB model, the message of the existence of the excluded volume is clear.<sup>29</sup>

## AUTHOR INFORMATION

### Corresponding Author

\*E-mail: turi@chem.elte.hu. Fax: 36-1-372-2592.

### Funding

This work was supported by a research grant to L.T. from the National Research Fund of Hungary (OTKA, K104237).

## Notes

The authors declare no competing financial interest.

## REFERENCES

- (1) Hart, E. J.; Boag, J. W. *J. Am. Chem. Soc.* **1962**, *84*, 4090–4095.
- (2) Hart, E. J.; Anbar, M. *The Hydrated Electron*; Wiley-Interscience: New York, 1970.
- (3) Garrett, B. C.; Dixon, D. A.; Camaioni, D. M.; Chipman, D. M.; Johnson, M. A.; Jonah, C. D.; Kimmel, G. A.; Miller, J. H.; Rescigno, T. N.; Rossky, P. J.; Xantheas, S. S.; Colson, S. D.; Laufer, A. H.; Ray, D.; Barbara, P. F.; Bartels, D. M.; Becker, K. H.; Bowen, H.; Bradforth, S. E.; Carmichael, I.; Coe, J. V.; Corrales, L. R.; Cowin, J. P.; Dupuis, M.; Eienthal, K. B.; Franz, J. A.; Gutowski, M. S.; Jordan, K. D.; Kay, B. D.; LaVerne, J. A.; Lyman, S. V.; Madey, T. E.; McCurdy, C. W.; Meisel, D.; Mukamel, S.; Nilsson, A. R.; Orlando, T. M.; Petrik, N. G.; Pimblott, S. M.; Rustad, J. R.; Schenter, G. K.; Singer, S. J.; Tokmakoff, A.; Wang, L.-S.; Wittig, C.; Zwiern, T. S. *Chem. Rev.* **2005**, *105*, 355–389.
- (4) Elkins, M. H.; Williams, H. L.; Shreve, A. T.; Neumark, D. M. *Science* **2013**, *342*, 1496–1499.
- (5) Buchner, F.; Schultz, T.; Lübcke, A. *Phys. Chem. Chem. Phys.* **2012**, *14*, S837–S842.
- (6) Siefermann, K. R.; Abel, B. *Angew. Chem., Int. Ed.* **2011**, *50*, 5264–5272.
- (7) Siefermann, K. R.; Liu, Y.; Lugovoy, E.; Link, O.; Faubel, M.; Buck, U.; Winter, B.; Abel, B. *Nat. Chem.* **2010**, *2*, 274–279.
- (8) Sagar, D. M.; Bain, C. D.; Verlet, J. R. *J. Am. Chem. Soc.* **2010**, *132*, 6917–6919.
- (9) Wang, C.-R.; Lu, Q.-B. *Angew. Chem., Int. Ed.* **2007**, *46*, 6316–6320.
- (10) Verlet, J. R. R.; Bragg, A. E.; Kammrath, A.; Cheshnovsky, O.; Neumark, D. M. *Science* **2005**, *307*, 93–96.
- (11) Hammer, N. I.; Shin, J.-W.; Headrick, J. M.; Diken, E. G.; Roscioli, J. R.; Weddle, G. H.; Johnson, M. A. *Science* **2004**, *306*, 675–679.
- (12) Nordlund, D.; Ogasawara, H.; Bluhm, H.; Takahashi, O.; Odelius, M.; Nagasono, M.; Pettersson, L. G. M.; Nilsson, A. *Phys. Rev. Lett.* **2007**, *99*, 217406.
- (13) Marsalek, O.; Uhlig, F.; VandeVondele, J.; Jungwirth, P. *Acc. Chem. Res.* **2012**, *45*, 23–32.
- (14) Herbert, J. M.; Jacobson, L. D. *Int. Rev. Phys. Chem.* **2011**, *30*, 1–48.
- (15) Turi, L.; Sheu, W.-S.; Rossky, P. J. *Science* **2005**, *309*, 914–917.
- (16) Turi, L.; Rossky, P. J. *Chem. Rev.* **2012**, *112*, S641–S674.
- (17) Schnitker, J.; Motakabbir, K.; Rossky, P. J.; Friesner, R. *Phys. Rev. Lett.* **1988**, *60*, 456–459.
- (18) Rossky, P. J.; Schnitker, J. *J. Phys. Chem.* **1988**, *92*, 4277–4285.
- (19) Barnett, R. N.; Landman, U.; Nitzan, A. *J. Chem. Phys.* **1988**, *89*, 2242–2256.
- (20) Sprik, M.; Klein, M. L. *J. Chem. Phys.* **1988**, *89*, 1592–1607.
- (21) Kotler, Z.; Neria, E.; Nitzan, A. *Comput. Phys. Commun.* **1991**, *63*, 243–258.
- (22) Webster, F.; Rossky, P. J.; Friesner, R. A. *Comput. Phys. Commun.* **1991**, *63*, 494–522.
- (23) Staib, A.; Borgis, D. *J. Chem. Phys.* **1995**, *103*, 2642–2655.
- (24) Boero, M.; Parrinello, M.; Terakura, K.; Ikeshoji, T.; Liew, C. C. *Phys. Rev. Lett.* **2003**, *90*, 226403.
- (25) Herbert, J. M.; Head-Gordon, M. *Proc. Natl. Acad. Sci. U.S.A.* **2006**, *103*, 14282–14287.
- (26) Frigato, T.; VandeVondele, J.; Schmidt, B.; Schütte, C.; Jungwirth, P. *J. Phys. Chem. A* **2008**, *112*, 6125–6133.
- (27) Marsalek, O.; Uhlig, F.; Frigato, T.; Schmidt, B.; Jungwirth, P. *Phys. Rev. Lett.* **2010**, *105*, 043002.
- (28) Barnett, R. N.; Giniger, R.; Cheshnovsky, O.; Landman, U. *J. Phys. Chem. A* **2011**, *115*, 7378–7391.
- (29) Uhlig, F.; Marsalek, O.; Jungwirth, P. *J. Phys. Chem. Lett.* **2012**, *3*, 3071–3075.
- (30) Uhlig, F.; Marsalek, O.; Jungwirth, P. *J. Phys. Chem. Lett.* **2013**, *4*, 338–343.

- (31) Uhlig, F.; Herbert, J. H.; Coons, M. P.; Jungwirth, P. *J. Phys. Chem. A* **2014**, *118*, 7507–7515.
- (32) Herbert, J. M.; Head-Gordon, M. *J. Phys. Chem. A* **2005**, *109*, 5217–5229.
- (33) Glover, W. J.; Casey, J. R.; Schwartz, B. J. *J. Chem. Theory Comput.* **2014**, *10*, 4661–4671.
- (34) Ogg, R. A. *J. Am. Chem. Soc.* **1946**, *68*, 155–155. Ogg, R. A. *Phys. Rev.* **1946**, *69*, 668–669.
- (35) Tuttle, T. R., Jr.; Golden, S. J. *J. Phys. Chem.* **1991**, *95*, 5725–5736.
- (36) Hameka, H. F.; Robinson, G. W.; Marsden, C. J. *J. Phys. Chem.* **1987**, *91*, 3150–3157.
- (37) Sobolewski, A. L.; Domcke, W. *J. Phys. Chem. Chem. Phys.* **2007**, *9*, 3818–3829.
- (38) Muguet, F. F. Investigations of Diffuse Intermolecular Electronic Systems. Ph.D. Thesis, Texas Tech University, Lubbock, TX, 1992.
- (39) Kevan, L. *Radiat. Phys. Chem.* **1981**, *17*, 413–423.
- (40) Schnitker, J.; Rossky, P. J. *J. Chem. Phys.* **1987**, *86*, 3471–3485.
- (41) Wallqvist, A.; Thirumalai, D.; Berne, B. J. *J. Chem. Phys.* **1987**, *86*, 6404–6418.
- (42) Jonah, C. D.; Romero, C.; Rahman, A. *Chem. Phys. Lett.* **1986**, *123*, 209–214.
- (43) Schnitker, J.; Rossky, P. J. *J. Chem. Phys.* **1987**, *86*, 3462–3470.
- (44) Barnett, R. N.; Landman, U.; Cleveland, C. L.; Jortner, J. *J. Chem. Phys.* **1988**, *88*, 4421–4428.
- (45) Turi, L.; Borgis, D. J. *Chem. Phys.* **2002**, *117*, 6186–6195.
- (46) Jacobson, L. D.; Herbert, J. M. *J. Chem. Phys.* **2010**, *133*, 154506.
- (47) Larsen, R. E.; Glover, W. J.; Schwartz, B. J. *Science* **2010**, *329*, 65–69.
- (48) Casey, J. R.; Kahros, A.; Schwartz, B. J. *J. Phys. Chem. B* **2013**, *117*, 14173–14182.
- (49) Turi, L.; Madarász, Á. *Science* **2011**, *331*, 1387–1387.
- (50) Jacobson, L. D.; Herbert, J. M. *Science* **2011**, *331*, 1387–1387.
- (51) Herbert, J. M.; Jacobson, L. D. *J. Phys. Chem. A* **2011**, *115*, 14470–14483.
- (52) Bartels, D. M. *J. Chem. Phys.* **2001**, *115*, 4404–4405.
- (53) Coe, J. V.; Williams, S. M.; Bowen, K. H. *Int. Rev. Phys. Chem.* **2008**, *27*, 27–51.
- (54) Griffin, G. B.; Young, R. M.; Ehrler, O. T.; Neumark, D. M. *J. Chem. Phys.* **2009**, *131*, 194302.
- (55) Barnett, R. N.; Landman, U.; Cleveland, C. L.; Jortner, J. *Phys. Rev. Lett.* **1987**, *59*, 811–814.
- (56) Barnett, R. N.; Landman, U.; Cleveland, C. L.; Jortner, J. *J. Chem. Phys.* **1988**, *88*, 4429–4447.
- (57) Madarász, Á.; Rossky, P. J.; Turi, L. *J. Chem. Phys.* **2009**, *130*, 124319.
- (58) Turi, L.; Madarász, Á.; Rossky, P. J. *J. Chem. Phys.* **2006**, *125*, 014308.
- (59) Jacobson, L. D.; Herbert, J. M. *J. Am. Chem. Soc.* **2011**, *133*, 19889–19899.
- (60) Berendsen, H. J. C.; Postma, J. P. M.; van Gunsteren, W. F.; Hermans, J. In *Intermolecular Forces*; Pullman, B., Ed.; Reidel: Dordrecht, The Netherlands, 1981; pp 331–342. Toukan, K.; Rahman, A. *Phys. Rev. B* **1985**, *31*, 2643–2648.
- (61) Turi, L. *J. Chem. Phys.* **2014**, *140*, 204317.
- (62) Voora, V. K.; Ding, J.; Sommerfeld, T.; Jordan, K. D. *J. Phys. Chem. B* **2013**, *117*, 4365–4370.
- (63) Morrison, M. A.; Collins, L. A. *Phys. Rev. A* **1978**, *17*, 918–938.
- (64) Phillips, J. C.; Kleinman, L. *Phys. Rev.* **1959**, *116*, 287–294.
- (65) Cohen, M. H.; Heine, V. *Phys. Rev.* **1961**, *122*, 1821–1826.
- (66) Smallwood, C. J.; Larsen, R. E.; Glover, W. J.; Schwartz, B. J. *J. Chem. Phys.* **2006**, *125*, 074102.
- (67) Turi, L.; Gageot, M.-P.; Levy, N.; Borgis, D. *J. Chem. Phys.* **2001**, *114*, 7805–7815.
- (68) Allen, M. P.; Tildesley, D. J. *Computer Simulation of Liquids*; Clarendon: Oxford, U.K., 1987.
- (69) Madarász, Á.; Rossky, P. J.; Turi, L. *J. Phys. Chem. A* **2010**, *114*, 2331–2337.
- (70) Marsalek, O.; Uhlig, F.; Jungwirth, P. *J. Phys. Chem. C* **2010**, *114*, 20489–20495.
- (71) We note that classification of excess electronic states (i.e., interior-state vs different surface states) based on the radii of gyration necessarily contains a certain degree of arbitrariness. For example, the radius of gyration of a uniform sphere is  $\sim 77\%$  of the physical radius of the sphere.
- (72) We note that this observation also holds for even smaller clusters ( $n = 20$  and  $30$ ), as seen from test simulations.
- (73) Makov, G.; Nitzan, A. *J. Phys. Chem.* **1994**, *98*, 3459–3466.
- (74) Tang, Y.; Shen, H.; Sekiguchi, K.; Kurahashi, N.; Mizuno, T.; Suzuki, Y.-L.; Suzuki, T. *J. Phys. Chem. Chem. Phys.* **2010**, *12*, 3653–3655.
- (75) Shreve, A. T.; Yen, T. A.; Neumark, D. M. *Chem. Phys. Lett.* **2010**, *493*, 216–219.
- (76) Ayotte, P.; Johnson, M. A. *J. Chem. Phys.* **1997**, *106*, 811–814.
- (77) Jou, F.-Y.; Freeman, G. R. *J. Phys. Chem.* **1977**, *81*, 909–915.
- Jou, F.-Y.; Freeman, G. R. *Can. J. Chem.* **1979**, *57*, 591–597.
- (78) We performed ab initio calculations on 100 configurations of the smaller cluster size ( $n = 12$ ) and 10 configurations of the larger cluster size ( $n = 24$ ). The text gives the average VDE values.
- (79) Frisch, M. J.; Trucks, G. W.; Schlegel, H. B.; Scuseria, G. E.; Robb, M. A.; Cheeseman, J. R.; Scalmani, G.; Barone, V.; Mennucci, B.; Petersson, G. A.; Nakatsuji, H.; Caricato, M.; Li, X.; Hratchian, H. P.; Izmaylov, A. F.; Bloino, J.; Zheng, G.; Sonnenberg, J. L.; Hada, M.; Ehara, M.; Toyota, K.; Fukuda, R.; Hasegawa, J.; Ishida, M.; Nakajima, T.; Honda, Y.; Kitao, O.; Nakai, H.; Vreven, T.; Montgomery, J. A., Jr.; Peralta, J. E.; Ogliaro, F.; Bearpark, M.; Heyd, J. J.; Brothers, E.; Kudin, K. N.; Staroverov, V. N.; Kobayashi, R.; Normand, J.; Raghavachari, K.; Rendell, A.; Burant, J. C.; Iyengar, S. S.; Tomasi, J.; Cossi, M.; Rega, N.; Millam, M. J.; Klene, M.; Knox, J. E.; Cross, J. B.; Bakken, V.; Adamo, C.; Jaramillo, J.; Gomperts, R.; Stratmann, R. E.; Yazyev, O.; Austin, A. J.; Cammi, R.; Pomelli, C.; Ochterski, J. W.; Martin, R. L.; Morokuma, K.; Zakrzewski, V. G.; Voth, G. A.; Salvador, P.; Dannenberg, J. J.; Dapprich, S.; Daniels, A. D.; Farkas, Ö.; Foresman, J. B.; Ortiz, J. V.; Cioslowski, J.; Fox, D. J. *Gaussian 09*, revision B.01; Gaussian, Inc.: Wallingford, CT, 2009.